Lee et al. *NPG Asia Materials* (2026)18:21
https://doi.org/10.1038/s41427-026-00650-x

NPG Asia Materials

ARTICLE Open Access

Significant phase deviation of magnetic quantum oscillations induced by magnetic impurities

Sang-Eon Lee[1,2], Sanghyun Ji[1,3], Junhee Park[4], Munir Humayun[4,5] and Myung-Hwa Jung[1]

Abstract

Magnetic quantum oscillations, such as Shubnikov-de Haas oscillations or de Haas-van Alphen oscillations, are widely used tools for fermiology. Notably, the phase of magnetic quantum oscillations could inform about the symmetry or topology of materials with careful analysis. However, the interpretation of the phase is usually much more subtle than that of the frequency, and unexpected phases are often observed, hindering the extraction of intrinsic information from the phases. Therefore, identifying the possible source of phase deviation is crucial for the proper interpretation of the phase. Here, we grew high-quality $NbSb_2$ single crystals with the exceptionally low residual resistivity of ~0.078 μΩ cm at $T = 2$ K, which enables us to detect the effect of a tiny amount of impurities in the de Haas-van Alphen effect. Unexpectedly, we observed a significant phase deviation around 0.58π induced by magnetic impurities, but no phase shift by nonmagnetic impurities. We explained the phase deviation by the modified Lifshitz-Kosevich formula incorporating magnetic scattering or spin-dependent scattering, which is supported by the imbalanced density of states between spin-up and -down impurity states calculated by the density functional theory. Our study showcases the effect of a tiny amount of magnetic impurities on the phase of magnetic quantum oscillations, giving an insight into the phase analysis and understanding the interaction between itinerant electrons and magnetic impurities.

Introduction

Magnetic quantum oscillations (MQOs) serve as a valuable tool for investigating the properties of the Fermi surface by measuring the resistance (Shubnikov-de Haas effect) or magnetization (de Haas-van Alphen effect) under varying applied magnetic fields. The frequency of MQOs provides the cross-sectional area of the Fermi surface, which enables us to estimate the size and shape of the Fermi surface. The Fermi surfaces of various materials, such as superconductors[1–6], topological materials[7–15], have been characterized. It is also noteworthy that MQOs can probe exotic states like Fermi arcs[16,17] or strongly correlated states[18,19].

As well as the frequency, the phase of MQOs also contains useful information. The earliest use of the phase information is the extraction of the *g*-factor[20–22]. Later, it turned out that the Berry phase of electron orbits could be informed by the phase analysis of Graphene[23,24]. With the emergence of topological materials, this concept has rapidly been extended to topological materials, and the nontrivial Berry phase has been claimed based on the phase analysis in topological insulators[25–29] and semimetals[7,15,30–36]. The interpretation of the phase has been further polished and related to the more fundamental concepts, such as topology/symmetry[37] and the zero field response function[38]. While the phase of MQOs contains a lot of information, it also indicates that the interpretation of the phase could be complicated in terms of distinguishing many contributions. Furthermore, unexpected phase deviations are often observed, for instance, from interband correlation[39] or inhomogeneity of the sample[40]. Therefore, identifying the possible source of phase deviation/contribution is crucial for the proper interpretation of the phase.

Here, we observed an unexpected and significant phase deviation of ~0.58π in the de Haas-van Alphen (dHvA) effect of high-quality $NbSb_2$ single crystals induced by a

Correspondence: Myung-Hwa Jung (mhjung@sogang.ac.kr)
[1]Department of Physics, Sogang University, Seoul, Republic of Korea
[2]National High Magnetic Field Laboratory, Tallahassee, FL, USA
Full list of author information is available at the end of the article
These authors contributed equally: Sang-Eon Lee, Sanghyun Ji

tiny amount of magnetic impurities of ~34 ppm per formula unit. With the time-reversal symmetry, the phase of dHvA oscillations should be confined to 0 or π (−π/4 or 3π/4 with the three-dimensional correction)[37]. This condition has been proved in $NbSb_2$ with the extensive study of the dHvA effects with varying the strength and direction of the magnetic fields[15]. Breaking of this condition by the introduction of dilute and paramagnetic impurities is unexpected since the paramagnets still preserve the time-reversal symmetry globally. On the other hand, we found the absence of phase deviation, where the phases are converged to −π/4, with nonmagnetic impurities.

We attribute this unexpected phase deviation by dilute magnetic impurities to the ultrahigh sample quality with the residual resistivity of ~0.078 μΩ cm at $T = 2$ K, which is highly sensitive to the effect of spin-dependent scattering between the itinerant electrons and magnetic impurities. The fundamental and second harmonics of the dHvA effects with the magnetic impurities are well fitted with the spin-dependent scattering model suggested in the previous reports[41–43], but we found that the spin-dependent scattering should be seen as a field-dependent phenomenon in our system. It is also notable that the considerable amplitude modulation has been observed in the previous cases[41–43], but our case with the dilute magnetic impurities only shows the significant phase deviation without notable amplitude modulation. This spin-dependent scattering scenario is also supported by our density functional theory (DFT) calculations, where the projected density of states (PDOS) of the Fe impurities reveals a pronounced peak in the minority spin channel near the Fermi level, accompanied by the imbalance of the density of state between majority and minority spin channels in $NbSb_2$.

Materials and methods

Sample synthesis

Here, we discuss six different single crystals with different dopants and doping ratios: a crystal without doping (Pristine), a Bi-doped crystal (Bi-d), a Cr-doped crystal (Cr-d), and three Fe-doped crystals (Fe-d1, Fe-d2, and Fe-d3). For the sample synthesis, Nb powder (99.99%), Sb shots (99.9999%), Bi needles (99.998%), Cr lumps (99.99%), and Fe powder (99.998%) were purchased from Alpha Aesar. The needles, lumps, and shots were carefully ground before being used for synthesis. Stoichiometries of $NbBi_xSb_{2-x}$ and $Nb_{1-x}(Fe, Cr)_xSb_2$ were sealed in quartz tubes in a vacuum environment with $x = 0.2$ for the Bi-d sample, $x = 0.1$ for the Cr-d sample, $x = 0.05$, 0.15, 0.3 for Fe-d1, Fe-d2, and Fe-d3 samples, respectively. For solid-state reaction, the quartz tubes were put into the box furnace at 700 °C for 36 h. For chemical vapor transport, 1 g of solid-reacted materials was put on one side of vacuum-sealed quartz tubes as source materials with 10 mg/cc of iodine as a transport agent. The temperature was set to 1000 °C for the source side and 900 °C for the other side for 7 days. Shiny crystals were obtained and elongated along the crystal *b*-axis. The crystals were bar-shaped before measurements, with typical dimensions of 3–5 mm for length, 0.5–2 mm for width, and 0.3–0.5 mm for depth.

Sample characterization

An Electron Probe Micro-Analyzer (EPMA) (JXA-8530F, JEOL Ltd, Japan) located at the National Center for Inter-University Research Facilities, Seoul National University, Republic of Korea, was used to investigate the chemical compositions of the samples with 15 keV and 20 nA electron beams. For all samples, the Nb:Sb ratio maintained 1:2 stoichiometry. For the dopants, only the heavy element Bi could be detected as 0.40(2)% per formula unit in the Bi-d sample, and other dopants' signals were too weak to be detected, indicating that all doping is within dilute limits. An X-ray diffraction spectroscopy (Rigaku DMAX 2500 diffractometer, Rigaku, Japan) with Cu Kα ($\lambda = 1.5406$ Å) radiation operated at 40 kV and 15 mA was used for investigating the crystal structure for powder specimens. The refinement gives $a = 10.2335(4)$ Å, $b = 3.6305(2)$ Å, $c = 8.3301(4)$ Å, and $\beta = 120.029(2)°$ with a monoclinic structure (space group: $C2/m$) for a pristine sample, which is consistent with previously reported values[44–47]. The refinement results of pristine, Bi-doped, and Cr-doped samples have been reported in ref. [40]. Note that the structural difference between pristine and doped samples is not significant.

The small doping ratios of Cr and Fe, which were not detected in EPMA, were investigated using a micro-X-Ray Fluorescence spectrometer (μXRF) (Bruker Nano GmbH, Berlin, Germany) located at the Center for Rare Earths, Critical Minerals, and Industrial Byproducts (RECMIB), National High Magnetic Field Laboratory, Florida State University, USA. The instrument is equipped with a Rh anode X-ray tube and polycapillary focusing optics, producing a focused beam with a nominal 20 μm spot size. Measurements were conducted under vacuum (~2 mbar) to enhance the detection of low-energy X-rays. The excitation voltage was varied between 20 and 50 kV, with the tube current automatically adjusted (typically 400–600 μA) by the instrument to maintain constant power. Primary beam filters (100 μm of Al, 100 μm of Ti, and 25 μm of Cu) are mounted internally to optimize excitation conditions across different energy ranges, thereby improving the signal-to-noise ratio (S/N) for the elements of interest. Each sample was analyzed at four or five distinct points, with an acquisition time of 300 s (5 min) per point. The acquired spectra were background-corrected and quantified using the fundamental parameter (FP) approach implemented in the Bruker M4 Tornado analysis software.

The atomic ratios of Pristine, Cr-d, and Fe-d3 samples confirmed through μXRF are listed in Supplemental Information Table S1 (we could not resolve the Fe doping ratio for Fe-d1 and Fe-d2). We clearly detected the Cr concentration in Cr-d, which is 562 ± 65 atomic ppm or 0.17 ± 0.20% per the formula unit. The instrumental background for Cr was less than 10 atomic ppm. For Fe concentration, we found instrumental background signals around 100–110 atomic ppm for Pristine and Cr-d samples. The Fe concentration of Fe-d3 yields 269 ± 30 atomic ppm, which is considerably larger than the instrumental background, revealing the real Fe concentration in Fe-d3. Taking 100 ppm for the instrumental background, we obtain 169 ± 30 atomic ppm or 0.05(1)% per the formula unit, for the Fe concentration of Fe-d3. Note that actual doping concentrations are considerably smaller than the nominal ratios used in the synthesis process, implying their higher formation energies.

Electrical transport and magnetization measurements

A commercial magnetic property measurement system with a superconducting quantum interference device-vibrating sample magnetometer (MPMS3 SQUID-VSM, Quantum Design) with a magnetic field range of −7-7 T and a temperature range of 1.8–400 K was used for magnetization measurements. In the magnetization measurements, the magnetic fields were applied along the crystal *b*-axis, and the magnetizations along the *b*-axis were measured. For electrical transport measurements, a commercial transport option for MPMS3 (Quantum Design) was used with a Keithley 2635A source measurement unit and a Keithley 2182A nanovoltmeter. The standard 4-probe and Hall configurations were used for the electrical contacts. The electric currents were applied along the crystal *b*-axis, and the magnetic fields were applied perpendicular to the current direction and normal to the surface where the electrical contacts are attached.

Density function theory calculation

First-principles calculations based on DFT were performed using the QUANTUM ESPRESSO package[48–50]. The Perdew–Burke–Ernzerhof exchange-correlation functional within the generalized gradient approximation (GGA) was employed[51,52]. The interactions between ions and valence electrons were described using Kresse–Joubert-type projector augmented-wave pseudopotentials[53] provided by the PSlibrary[54]. The plane-wave kinetic energy cutoff and charge density cutoff were set to 120 Ry and 720 Ry, respectively. Structural optimizations were carried out until the force on atoms and the total stress converged to below 1.0×10^{-5} Ry and 0.1 kbar, respectively. For band structure calculation of pristine $NbSb_2$, a Monkhorst–Pack *k*-point mesh[55] of 8 × 8 × 5 was employed. A denser 40 × 40 × 25 *k*-point grid was used in the non-self-consistent field calculation to obtain Fermi surface. The obtained Fermi surface was analyzed by SKEAF code[56,57], which can evaluate MQO frequency and effective masses for various magnetic field directions. Fe- and Cr-doped systems were modeled by replacing one Nb or Sb atom or placing one Fe or Cr atom in interstitial sites within the same 3 × 2 × 2 supercell. We used norm-conserving pseudopotentials from Pseudo-Dojo[58] for the following calculations to ensure compatibility with potential future calculations in other codes. Spin-polarized calculations were performed for doped systems with an initial magnetic moment of 1.0 μ_B assigned to the Fe or Cr atom. To describe the strong correlation between electrons in Fe or Cr 3*d* orbital, the Hubbard *U* correction was introduced with Dudarev approach of GGA+*U*[59]. All calculations were performed without spin-orbit coupling (SOC), unless otherwise noted. Atomic structures were visualized using VESTA[60], and Fermi surfaces were plotted using FermiSurfer[61].

Results and discussion

Drastic effect of dilute dopants on the electrical properties of $NbSb_2$

The effects of dilute Bi, Cr, and Fe doping were studied with electrical transport measurements. All dopants dramatically reduced the magnetoresistance (MR) and Hall resistivity of $NbSb_2$, which are shown in Fig. 1a, b, respectively. The MR of Pristine reaches ≈ 1,230,000% at $T = 2$ K and $B = 7$ T. Similar large and nonsaturating MR has been reported in previous studies of $NbSb_2$[15,44,45,47,62]. The MR values of doped $NbSb_2$ are MR ≈ 4260, 324, 1180, 70, and 33% for Bi-d, Cr-d, Fe-d1, Fe-d2, and Fe-d3, respectively. The decreases in the MR values imply decreases in the mobilities since the semiclassical MR ratio is proportional to $\mu_t^2 B^2$, where μ_t is the transport mobility[63]. The magnitude of Hall resistivities also decreases by doping, and shows negative slopes, indicating the electron dominance.

We fitted the MR and Hall resistivities with the two-carrier model[63] whose fitting parameters yield the carrier densities of ≈2.369(7) and $2.368(7) \times 10^{20}$ cm^{-3} and the high mobilities of ≈21.6(1) and 12.2(1) m^2/Vs for electron and hole of Pristine, respectively. The results of the two-carrier fitting for all samples and related discussion can be found in Supplemental Information including Note 1, Fig. S1, and Table S2 (see also refs. [64–69] therein). For Pristine, the electron and hole carrier densities indicate a nearly perfect electron-hole compensation of $n_e/n_h \approx 1.0004$, which has been reported in a previous DFT calculation for $NbSb_2$[70]. Note that many topological semimetals representing extremely high magnetoresistances also have compensated electron-hole carrier densities, as reported in WTe_2[71], W(Mo)P_2[72], and ZrSiS[73].

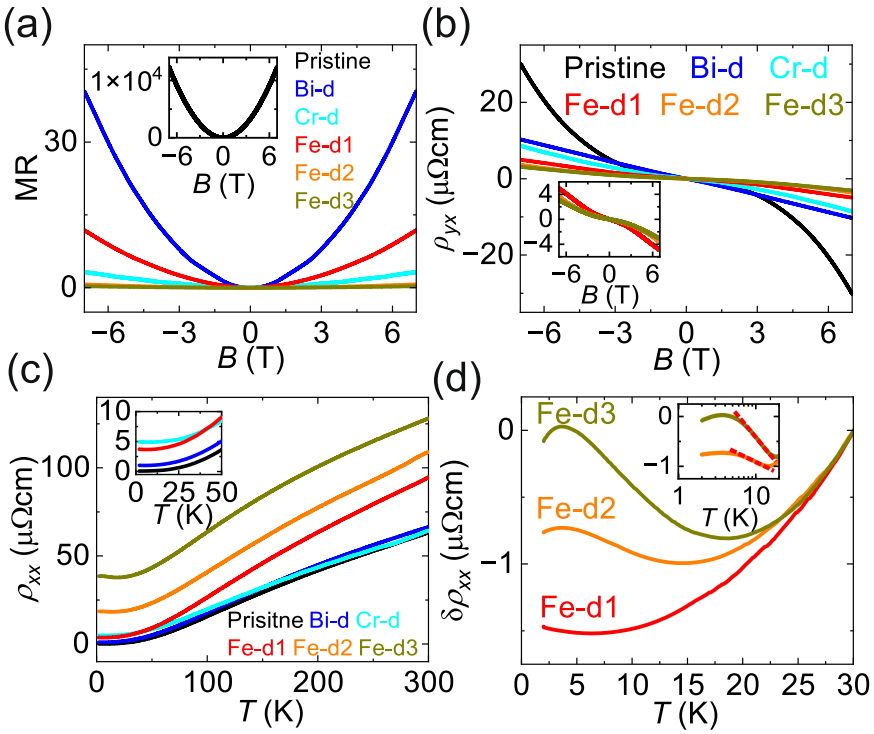

Fig. 1 Electrical transport properties of pristine, Bi-, Cr-, and Fe-doped $NbSb_2$. **a** MR ratios, $[\rho_{xx}(B) - \rho_{xx}(B=0)]/\rho_{xx}(B=0)$, of Bi-d, Cr-d, Fe-d1, Fe-d2, and Fe-d3 at $T = 2$ K. Inset: MR ratio of Pristine at $T = 2$ K. **b** Hall resistivities, ρ_{yx}, at $T = 2$ K. Inset: Magnified view of Hall resistivities focusing on Fe-d1, Fe-d2, and Fe-d3. **c** Temperature-dependent resistivities. Inset: Magnified view for the low-temperature regime, focusing on Pristine, Bi-d, Cr-d, and Fe-d1. **d** Temperature-dependent resistivity differences, $\delta\rho_{xx} \equiv \rho_{xx}(T) - \rho_{xx}(T = 30\,\text{K})$, of Fe-d1, Fe-d2, and Fe-d3. Inset: Plot of temperature-dependent resistivity differences of Fe-d2 and Fe-d3 with a logarithm scale of temperature. The red dashed lines display the linear fitting lines in the ranges of 6-13 and 7-15 K for Fe-d2 and Fe-d3, respectively.

According to decreases in MR, the dopants significantly increase the residual resistivity (RR). Figure 1c shows the temperature-dependent resistivities. The RR value at $T = 2$ K of Pristine reaches RR ≈ 0.078 μΩ cm, which increases to RR ≈ 1.03, 4.95, 3.72, 18.5, and 38.5 μΩ cm for Bi-d, Cr-d, Fe-d1, Fe-d2, and Fe-d3, respectively (see the inset of Fig. 1c). Accordingly, the residual resistivity ratio (RRR), which is defined by $\rho_{xx}(T = 300\,\text{K})/\rho_{xx}(T = 2\,\text{K})$, decreases by doping from RRR ≈ 812 of Pristine to RRR ≈ 64.5, 13.0, 25.4, 5.9, and 3.3 of Bi-d, Cr-d, Fe-d1, Fe-d2, and Fe-d3, respectively. All these changes of MR, RR, and RRR by doping suggest that the dopants introduce disorders and act as scattering centers. Note that similar behavior can be found in a systematic substitution study of $Nb_{1-x}Ta_xSb_2$ system[74]. The values of MR, Hall resistivity, RR, and RRR are listed in Table 1. We emphasize that the doping ratio is small enough not to be detected by the resolution of EPMA except for the Bi-d sample. The dramatic effects in MR, Hall, and RR indicate that the pristine $NbSb_2$ is an exceptionally clean host material, which has a high sensitivity to introduced impurities in its electrical properties.

Table 1 Residual resistivity (RR), residual resistivity ratio (RRR), magnetoresistance (MR) ratio, Hall values of Pristine, Bi-, Cr, and Fe-doped $NbSb_2$.

	MR at 7 T	Hall at 7 T (μΩ cm)	RR (μΩ cm)	RRR
Pristine	12,300	−30.19	0.078	812
Bi-d	42.6	−10.29	1.03	64.5
Cr-d	3.24	−8.63	4.95	13.0
Fe-d1	11.8	−4.95	3.72	25.4
Fe-d2	0.70	−3.65	18.5	5.9
Fe-d3	0.33	−3.10	38.5	3.3

The RR values are taken at 2 K and RRR is defined as $\rho_{xx}(T = 300\,\text{K})/\rho_{xx}(T = 2\,\text{K})$. The MR and Hall values are taken at 2 K.

Some distinctive behaviors are observed in the temperature-dependent resistivities of Fe-doped samples. The resistivities of Fe-doped samples increase faster with increasing temperature than the other samples. For instance, the resistivity of Fe-d1 is smaller than that of Cr-d at $T = 2$ K but becomes notably larger at $T = 300$ K. Furthermore, Fe-doped samples show the resistivity upturns

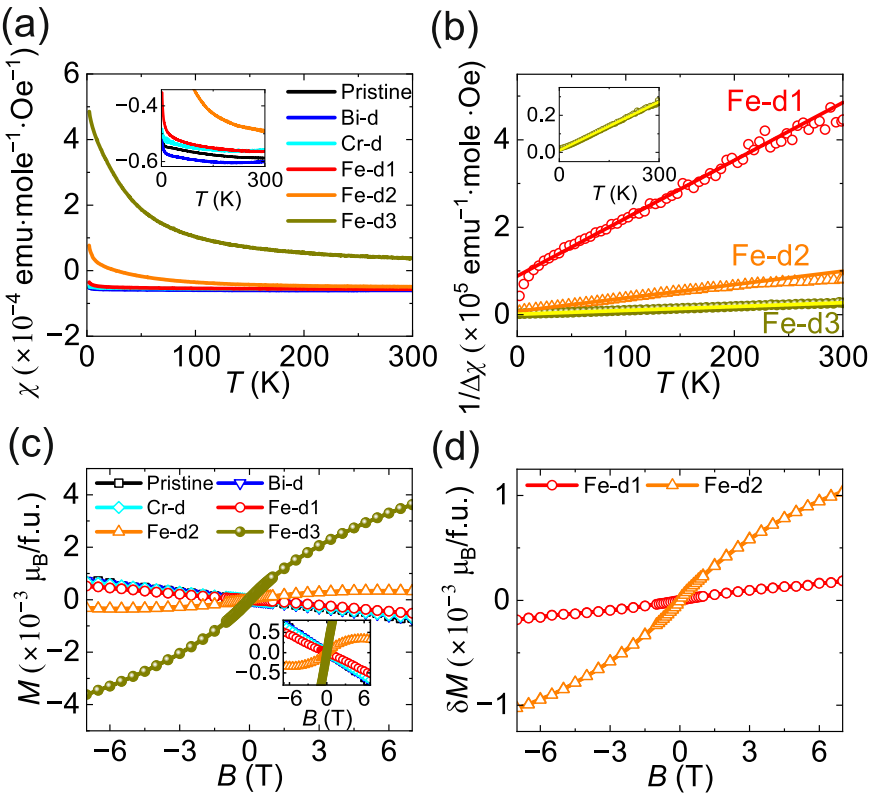

Fig. 2 Magnetic properties of pristine, Bi-, Cr-, and Fe-doped $NbSb_2$. a Temperature-dependent magnetic susceptibilities under the applied magnetic field of $B = 1$ T. Inset: Magnified view focusing on Pristine, Bi-d, Cr-d, and Fe-d1 samples. **b** Inverse of magnetic susceptibilities after subtracting temperature-independent magnetic susceptibilities χ_0, $1/\Delta\chi$ ($\Delta\chi \equiv \chi - \chi_0$), of Fe-1d, Fe-d2, and Fe-d3 as a function of temperature (the open circles) and the Curie–Weiss fitting lines (the solid lines), respectively. The χ_0 values of -5.86×10^{-5},-6.14×10^{-5}, and 5.58×10^{-7} emu·mole^{-1}·Oe^{-1} were subtracted from the magnetizations of Fe-1d, Fe-2d, and Fe-3d, respectively, to produce linear curves. The fitting yields the Curie–Weiss temperatures of $\theta_{CW} = -67(1)$,$-24.6(2)$, and $-11.8(3)$ K for Fe-d1, Fe-d2, and Fe-d3, respectively. The linear regimes span temperature ranges of around $T = 50$–250, 25–170, and 45–300 K for Fe-d1, Fe-d2, and Fe-d3, respectively, which are used for the fitting. Inset: Magnified view focusing on Fe-d3. **c** Field-dependent magnetizations at $T = 2$ K. Inset: Magnified view focusing on Pristine, Bi-d, Cr-d, Fe-d1, and Fe-d2. **d** Differences in magnetization of Fe-1d and Fe-2d from the magnetization of Pristine, δM (B) $\equiv M_{\text{Fe-d1,2}}$ (B) $- M_{\text{Pristine}}$ (B) at $T = 2$ K.

mimicking the Kondo effect characterized by $\rho_{xx} \propto -\ln T$[75–77]. Figure 1d shows the temperature-dependent resistivity difference, $\delta\rho_{xx} \equiv \rho_{xx}(T) - \rho_{xx}(T = 30\,\text{K})$, which provides a magnified view of the resistivity variance in the low-temperature regime. The upturn behavior becomes pronounced as the Fe doping ratio increases from Fe-d1 to Fe-d3, and the behaviors of $\rho_{xx} \propto -\ln T$ for Fe-d2 and Fe-d3 are shown in the inset of Fig. 1d. These results suggest the magnetic moments of Fe dopants interacting with the itinerant electrons. Interestingly, the upturn behaviors change to the downturn by further decreasing temperature, which can be explained by the coherent Kondo effect as reported in $Ce_{1-x}La_xCoIn_5$[78,79], $Ce_{1-x}La_xNi_2Ge_2$[80], and P-doped silicon[81]. However, verifying the exact origin of the downturn requires further investigation.

Localized magnetic moments of Fe-doped $NbSb_2$

The magnetic properties of pristine and doped $NbSb_2$ were investigated by measuring the magnetizations with varying temperature and applied magnetic fields. The temperature-dependent magnetic susceptibilities are shown in Fig. 2a. Pristine shows a diamagnetic signal with little temperature dependence. Considerable contributions of the positive magnetic susceptibilities, which sharply increase as temperature decreases, are observed in the Fe-doped samples, while the Bi- and Cr-doped samples do not show recognizable contributions of positive magnetic susceptibilities (see the inset of Fig. 2a). The positive magnetic susceptibility increases from Fe-d1 to Fe-d3, indicating the increasing Fe doping ratio from Fe-1d to Fe-d3. Note that Cr and Fe dopants both have 3*d* electrons as their valence electrons, but the magnetic behaviors are different, which might be attributed to the difference in interaction between the localized *d* electrons and the surrounding itinerant electrons[75,82,83].

We analyzed the magnetic susceptibilities of Fe-doped samples based on the Curie–Weiss law, which is given by $\Delta\chi \equiv \chi - \chi_0 = C/(T - \theta_{CW})$. The Curie constant C is given

by $C = N\mu_{eff}^2/3k_B$, where N is the magnetic atom density, μ_{eff} is the effective magnetic moment, and k_B is the Boltzmann constant. The variable χ_0 is introduced to incorporate the temperature-independent magnetic susceptibility, and the positive (negative) Curie–Weiss temperature, θ_{CW}, indicates the existence of (anti-) ferromagnetic coupling. We plotted $1/\Delta\chi$ vs. T, which is shown in Fig. 2b. Based on the Fe concentration of $N = 0.05\%$ per the formula unit in Fe-d3 obtained from the μXRF measurement, the Curie–Weiss fitting yields $\mu_{eff} = 3.0\ \mu_B$ and $\theta_{CW} = -12$ K for Fe-d3. The Curie–Weiss fitting was conducted for Fe-d1 and Fe-d2 as well, with fixed $\mu_{eff} = 3.0\ \mu_B$, yielding $N = 0.0034$ and 0.015% per the formula unit, and $\theta_{CW} = -67$ and -24 K for Fe-d1 and Fe-d2, respectively. Interestingly, we obtained negative values of θ_{CW} for all samples. These negative values of θ_{CW} indicate the antiferromagnetic coupling between localized magnetic moments, possibly driven by the Ruderman–Kittel–Kasuya–Yosida interaction[84–86]. Alternatively, the negative values of θ_{CW} can be interpreted as a result of antiferromagnetic exchange fields exerted by an itinerant electron cloud surrounding the magnetic impurities, which has been theoretically shown[76,87] and reported in many other Kondo materials[88–92]. In either case, the negative values of θ_{CW} evidence the interaction between the localized magnetic moments and the itinerant electrons. The field-dependent magnetizations of Fe-doped samples are not saturated up to $B = 7$ T at $T = 2$ K, which is shown in Fig. 2c, d. For Fe-d1 and Fe-d2, the nonmagnetic backgrounds were subtracted using the magnetization of Pristine to extract the pure magnetic signals from the Fe dopants, which is denoted by δM. This behavior contrasts with saturating Brillouin function-shaped magnetizations expected for localized magnetic moments, suggesting the interplay between the localized magnetic moments and itinerant electrons.

Significant phase deviation in the dHvA effects of Fe-doped $NbSb_2$

Clear dHvA effects observed in pristine and doped $NbSb_2$ allow us to investigate the effect of dopants on the Fermi surfaces. The oscillatory parts of the magnetizations after subtracting the sublinear background signals and their fast Fourier transform (FFT) spectra for Pristine, Bi-d, Cr-d, and Fe-d1 are shown in Fig. 3a, b, respectively. From the FFT spectra, we labeled the peaks of ζ (~198 T), α (~383 T), β (~705 T), and 2β (~1400 T). From Onsager's formula of $S = 2\pi eF/\hbar$[93], where S is an extremal cross-section area of the Fermi surface subjected to the normal plane of the magnetic field direction, F is the frequency of the oscillations, and $\hbar$ is the reduced Planck constant, we found $S = 0.0673$ Å^{-2} for the β peak. We roughly estimated the electron carrier density from S, assuming two spin-degenerate spherical electron pockets, yielding 2.12×10^{20} cm^{-3}, which is aligned with the electron carrier density of $2.369(7) \times 10^{20}$ cm^{-3} estimated from Pristine with the two-carrier model. Note that there is no observable dHvA effect for Fe-d3 and only β peak is barely observable in the FFT spectrum for Fe-d2. This implies that the scattering centers (defects from Fe dopants) subsequently increase as the Fe doping ratio increases from Fe-d1 to Fe-d3, leading to the suppression of dHvA effects.

For a deeper analysis, we separated the most predominant oscillations corresponding to β peak using an FFT bandpass filter; hereafter, we only deal with the β oscillations. We used the Lifshitz-Kosevich formula[94], which is given by

$$\Delta M^p(B) \approx -2A_0\sqrt{B}\frac{R_T^p R_D^p}{p^{3/2}}\left|\cos\frac{\pi p g m_c}{2m_e}\right|\sin\left[2\pi p\left(\frac{F}{B}-\frac{1}{2}\right)+\Theta^p-\frac{\pi}{4}\right], \quad (1)$$

where p is the harmonics index, A_0 is the dimensional constant, R_T^p is the temperature-reduction factor, R_D^p is the Dingle-reduction factor, m_c is the cyclotron mass, and m_e is the bare electron mass. The phase Θ is determined by $\Theta^p \equiv \frac{\pi}{2}[1 - \mathrm{sign}(\cos\frac{\pi p g m_c}{2m_e})]$, the temperature-reduction factor is given by $R_T^p = (2p\pi^2 m_c k_B T/e\hbar B)/\sinh(2p\pi^2 m_c k_B T/e\hbar B)$, and the Dingle-reduction factor is given by $R_D^p = \exp(-p\pi m_c/\tau eB)$, where τ is the relaxation time.

First, we draw the Landau fan diagram[94] to extract the frequencies and phases accurately. We assigned quarter integers, $N \equiv n + 1/4$ $(n + 3/4)$, to the magnetic field values at the minima (maxima) of oscillations, $B_{\min(\max)}$, and draw $1/B_{\min(\max)}$ vs. N plots, which are shown in Fig. 3c. The positive integers of n are assigned to have the x-intercepts of the Landau fan diagrams in the range of (−0.5, 0.5). For an accurate analysis, we corrected the magnetic field values considering the magnetic field error of our superconducting magnet. The correction procedure and related discussion are presented in Supplemental Information including Note 2, Fig. S2 and Table S3 (see also ref. [95] therein). We fitted the Landau fan diagrams with linear lines, whose slope and x-intercept are $1/F$ and $\gamma = -0.5 + \phi + \Theta^p/2\pi - 0.125$, respectively. The fitting yields $F = 704.218(3)$, 708.58(1), 717.1(1), and 704.94(1) T and $\gamma = -0.123(1)$, −0.111(3), −0.13(2), and +0.165(3) for Pristine, Bi-d, Cr-d, and Fe-d1, respectively. The small difference in the frequencies between the samples suggests that the doping ratios are diluted so as not to change the overall Fermi surface sizes significantly. The γ values of nonmagnetic Pristine, Bi-d, and Cr-d converge to -0.125, indicating $\Theta^p/2\pi = 0.5$. Interestingly, a large deviation of γ from those of nonmagnetic counterparts is observed in magnetic Fe-d1.

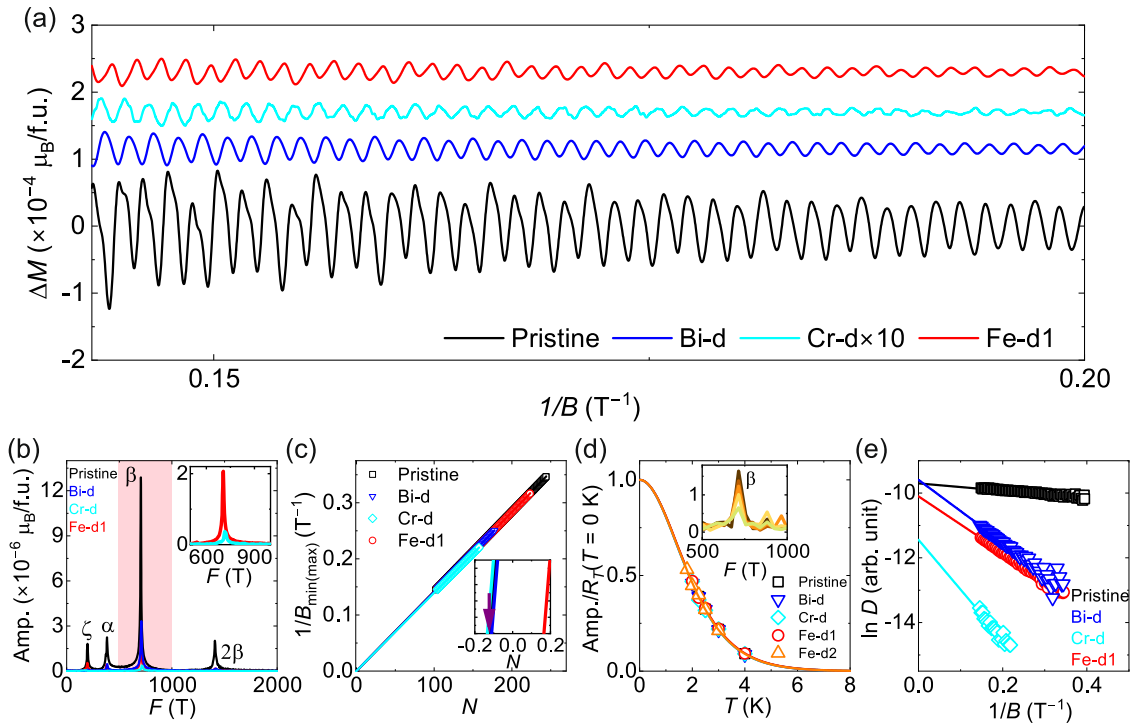

Fig. 3 dHvA effects of Pristine, Bi-, Cr-, and Fe-doped $NbSb_2$. a Magnetizations of Pristine, Bi-d, Cr-d, and Fe-d1 after subtracting sublinear background signals, displaying the dHvA effects at $T = 2$ K. The signal of Cr-d was magnified ten times for visibility. **b** Fast Fourier transform (FFT) spectra of the dHvA effects for Pristine, Bi-d, Cr-d, and Fe-d1 at $T = 2$ K. The peaks of ζ, α, β, and 2β are identified. The red shaded area shows the FFT bandpass filter range to separate β oscillations. Inset: Magnified view of Cr-d and Fe-d1's FFT spectra. The unit of the *y*-axis is the same as that of the main figure. **c** Landau fan diagrams of β oscillations and linear fitted curves of Pristine, Bi-d1, Cr-d1, and Fe-d1 at $T = 2$ K. Inset: Magnified view focusing on the *x*-intercepts. The purple arrow points $N = -0.125$. The unit of the *y*-axis is the same as that of the main. **d** Normalized temperature-dependent amplitudes of β oscillations under applied magnetic field of $B = 6.5$ T and fitted curves with the temperature reduction factor. The normalization is done by dividing the temperature-dependent amplitudes by R_T ($T = 0$ K). Inset: Temperature-dependent FFT spectra of Fe-d2, focusing on β peaks. The temperatures are 1.8, 2, 2.25, 2.5, and 3 K from the highest to the lowest peak amplitude. The unit of the *y*-axis is the same as that of **b**. **e** Dingle plot of β oscillations and linear fitted curves for Pristine, Bi-d, Cr-d, and Fe-d1 at $T = 2$ K.

The cyclotron masses were estimated by fitting the temperature-dependent amplitudes of dHvA effects with R_T (see Fig. 2d), yielding $m_c = 0.514(5)$, 0.513(5), 0.514(2), 0.51(1), and 0.51(2)m_e for Pristine, Bi-d, Cr-d, Fe-d1, and Fe-d2, respectively. The small difference in m_c again suggests that the Fermi surfaces are robust against dilute doping. The Dingle analysis[8,26,29,40,96] was conducted to estimate the relaxation times. The amplitudes of the dHvA effects were divided by $\sqrt{B}R_T$ which was defined as $D = \text{Amp.}/\sqrt{B}R_T$ which is proportional to R_D. We draw the Dingle plots, ln D as vs. $1/B$, which is shown in Fig. 3e. We fitted the Dingle plot with linear lines, whose slopes and intercepts give $-\pi m_c/\tau e$, respectively. The fitting yields $\tau = 7.8(1)$, 0.951(6), 0.61(2), and 1.05(1) ps for Pristine, Bi-d, Cr-d, and Fe-d1, respectively. Accordingly, the quantum mobility $\mu_q = e\tau/m_c$ was estimated as $\mu_q = 2.7$, 0.33, 0.21, and 0.36 m^2/Vs for Pristine, Bi-d, Cr-d, and Fe-d1, respectively. Note that μ_q of Pristine is considerably smaller than $\mu_e \approx 21.6\ m^2$/Vs obtained from the transport measurement, suggesting a suppression of large-angle or back scattering[97]. The suppression of large-angle or back scattering has been reported in other topological semimetals of Cd_3As_2[31] and W(Mo)P_2[72]. The parameters of β oscillations obtained from the dHvA analyzes are listed in Table 2.

The same analysis was conducted for the ζ oscillations for Pristine and Fe-d1. For Bi-d and Cr-d, the ζ oscillations are not large enough to analyze. Note that the analysis of α oscillations is not feasible since other oscillations overlap with it (see η oscillations in ref. [15]) The analysis of the ζ oscillations (see Fig. S3) yields $F = 197.39(3)$ and 196.9(4) T, $\gamma = -0.124(7)$ and $-0.18(7)$, $m_c = 0.66(2)m_e$ and 0.68(4)m_e, and $\tau = 2.7(1)$ and 1.45(7) ps for Pristine and Fe-d1, respectively. Interestingly, the phase deviation is small and within the fitting error range, and the difference in τ is also small compared to that of β oscillations. This indicates that the Fe localized magnetic moments selectively interact with β oscillations. It turns out that the β oscillations are from the electron pockets

Table 2 Parameters of the dHvA analyses.

	F (T)	γ	m_c (m_e)	τ (ps)	μ_q (m^2/Vs)	g
Pristine	704.218(3)	−0.123(1)	0.514(5)	7.8(1)	2.7	2.2032(3)
Bi-d	708.58(1)	−0.111(3)	0.513(5)	0.951(6)	0.33	2.22583(6)
Cr-d	717.1(1)	−0.13(2)	0.514(2)	0.61(2)	0.21	1.98633(3)
Fe-d1	704.94(1)	0.165(3)	0.51(1)	1.05(1)	0.36	1.9471(3)
Fe-d2	714	--	0.51(2)	--	--	--

F and m_c values of Fe-d2 are both obtained from the FFT spectra with the magnetic field range of $B = 6$-7 T, while those values of other samples are obtained from the Ladan fan diagrams and oscillations' amplitudes at $B = 6.5$, respectively.

and ζ oscillations are from the hole pockets in our DFT calculation, which will be discussed later, demonstrating that the Fe magnetic moments have a much more active interaction with the electrons compared to the holes. For reproducibility check, we repeated measurements and analyzed the ζ and β oscillations of an additional Fe-doped sample, whose magnetic behavior is similar to that of Fe-d1 (see Fig. S4). The phase shift of β oscillations was also observed in the additional sample, confirming that the phase shift is an intrinsic behavior.

To explain the phase shift of Fe-d1 and estimate the g factors, we directly fitted the first and second harmonics of the dHvA effect, which are shown in Fig. 4. The second harmonics are separated by an FFT bandpass filter with the range of 1000–2000 T. Unfortunately, the sizes of the second harmonics are not big enough to analyze for Bi-d and Cr-d, but fitting the first harmonics only was sufficient to estimate their g factors. We used Eq. (1) for nonmagnetic Pristine, Bi-d, and Cr-d, and used a spin-resolved model for Fe-d1 to incorporate the effect of the localized magnetic moments. On the other hand, we modified a previous model, incorporating spin-dependent scattering[41–43] for Fe-d1. We emphasize two major differences between our case and the previous cases[41–43]. In the previous model, they adopted the spin-dependent scattering rate $\Gamma_s = \Gamma + s\Delta\Gamma/2$, where s is the spin index with $+1$ or -1 for opposite spins, Γ is the average scattering rate over spins, and $\Delta\Gamma$ is the difference in scattering rates between opposite spins. While the previous model assumed field-independent $\Delta\Gamma$, we added linear field-dependence in $\Delta\Gamma$ as $\Delta\Gamma = \Gamma_0 + \Gamma_1 B$. Furthermore, while the previous results with the spin-dependent scattering showed pronounced amplitude modulation of the dHvA effects as a function of magnetic field, the behavior of the amplitude of Fe-d1 is almost indistinguishable from those of nonmagnetic counterparts, as shown in Fig. 2e, producing more experimental subtlety attributed to the diluteness of the dopant. Our modified Lifshitz–Kosevich formula for a dilute magnetic system is given by

$$\Delta M^p(B) \approx -A_0\sqrt{B}\frac{R_T^p}{p^{3/2}}\sum_{s=\pm} R_{D,s}^p \sin\left[2\pi p\left(\frac{F}{B}-\frac{1}{2}+s\frac{g_{eff}m_c}{4m_e}\right)-\frac{\pi}{4}\right], \quad (2)$$

where the Dingle reduction factor is now spin-dependent: $R_{D,s}^p = \exp(-p\pi m_c\Gamma_s/eB)$.

In the analysis, the effective masses of all samples analyzed here and the relaxation time of Pristine, Bi-d, and Cr-d are fixed with the obtained values from the analyzes shown in Fig. 3d, e, respectively. Subsequently, we simultaneously fitted the first and second harmonics of Pristine with Eq. (1), which yields $F = 704.2239(2)$ T, $A_0 = 0.0001593(2)$ μ_B/f.u. $T^{-1/2}$, and $g = 2.2032(3)$. The amplitude parameter A_0 is proportional to $F(\partial S/\partial\kappa)^{-1/2}$ [94], where κ is the momentum component parallel to the field direction. Given the similar values of F and m_c across the samples, it is reasonable to assume that the values of A_0 are also similar across them. Fixing A_0, the first harmonics of Bi-d and Cr-d were fitted with Eq. (1), as well as the first and second harmonics of Fe-d1 were simultaneously fitted with Eq. (2). The fitting yields $F = 708.6653(2)$, 716.995(1), and 705.114(2), $g = 2.22583(6)$, 1.98633(3), and 1.9471(3), respectively for Bi-d, Cr-d, and Fe-d1, $\Gamma = 0.977(1)$ ps^{-1} ($\tau = 1/\Gamma \approx 1.024$ ps), and $\Delta\Gamma = -0.0025(6)$ $ps^{-1} + 0.02993(4)B$ T^{-1} ps^{-1} for Fe-d1. The ratio of $\Delta\Gamma/\Gamma$ of Fe-d1 reaches 21.2% at $B = 7$ T. Note that $\Delta\Gamma$ of Fe-d1 depends almost linearly on B. Since $\Delta\Gamma$ requires an imbalance between spin up and down populations of localized magnetic moments, it might follow the magnetic polarization of the localized magnetic moments, which is almost linear with respect to B in the case of Fe-d1 (see Fig. 2d). The values of frequencies are almost the same as the values obtained from the Landau fan diagram, while it is interesting that the g factor values can be grouped into Pristine/Bi-d and Cr-d/Fe-d1. The significant change in the g factors of Cr-d/Fe-d1 might be attributed to the influence of localized 3d electrons. Although Cr-d does not show significant positive magnetic susceptibility, the reduced g factor implies that the 3d electrons still affect the itinerant electrons magnetically.

The role of magnetic scattering on the phase shift is more clearly displayed with the simulation, which can be found in Fig. S5. We simulated the dHvA effects of Fe-d1 with the magnetic scattering using the fitting parameters obtained, and without the magnetic scattering by setting the fitting parameters Γ_0 and Γ_1, which are relevant to the magnetic scattering, to zero. Interestingly, we found that the magnetic scattering produces considerable amplitude and phase changes for the first harmonics, but the effect is minor for the second harmonics. It turns out that the first (second) harmonics is at the condition of nearly

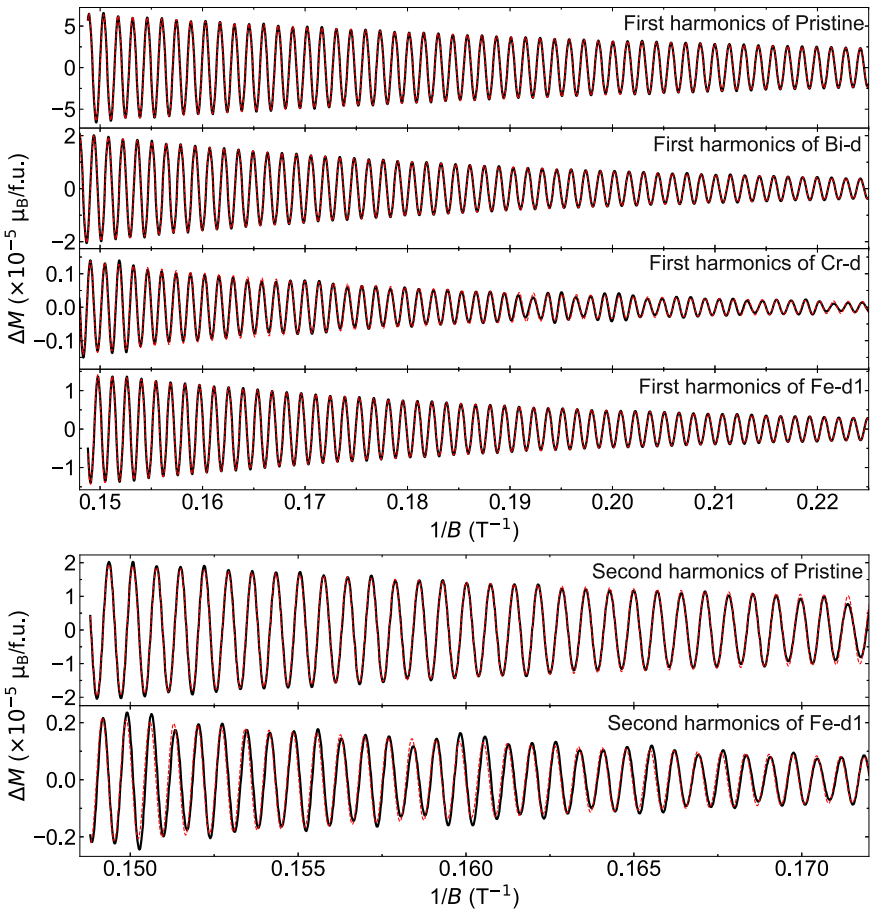

Fig. 4 First and second harmonics of the dHvA effects for pristine, Bi-, Cr-, and Fe-doped $NbSb_2$. The black solid lines and red dashed lines represent the data and fitted curves, respectively. The first and second harmonics of Pristine are simultaneously fitted with Eq. (1), yielding $A_0 = 0.0001593(2)$, $F = 704.2239(2)$ T, and $g = 2.2032(3)$. The parameter A_0 is fixed with Pristine's value for other samples. The first harmonics of Bi-d and Cr-d are fitted with Eq. (1), yielding $F = 708.6653(2)$ and 716.995(1) T, and $g = 2.22583(6)$ and 1.98633(3), respectively. The first and second harmonics of Fe-d1 are simultaneously fitted with Eq. (2), yielding $F = 705.144(2)$, $\Gamma = 0.977(1)$ ps^{-1}, $\Delta\Gamma = -0.0025(6)$ ps$^{-1} + 0.02993(4)B$ T^{-1} ps^{-1}, and $g = 1.9471(3)$.

destructive (constructive) interference between the spin up and down oscillations, which is (in-)sensitive to the magnetic scattering. Note that the interference between the spin up and down oscillations is determined by the phase difference $p\pi g_{eff} m_c/m_e$ for pth harmonics, which can be deduced from Eq. (2).

Density functional theory calculation of pristine and Fe-doped $NbSb_2$

To understand the magnetizations and correlation effects observed in Fe-doped $NbSb_2$, we performed first-principles calculations based on DFT. Figure 5a, b shows the electronic structure and Fermi surfaces of $NbSb_2$, respectively. Without the spin-orbit coupling, there are several band crossings near the Fermi level, which are gapped out by the spin-orbit coupling, forming the massive Dirac structure. This behavior has been pointed out in the previous electronic structure calculation[70]. For the carrier pockets, we found two identical ellipsoidal-shaped pockets for electron and one large irregular-shaped pocket and another small ellipsoidal-shaped pocket for hole, which have been shown in previous studies[44,47].

The Fermi surface was further analyzed by SKEAF code[56,57] to confirm that our Fermi surfaces are consistent with the experimental results (see Supplementary Note 3 for the details). The cyan ellipsoids correspond to massive Dirac electrons located around the L-I line in the band diagram. The calculated MQO frequency for these pockets is 901 T, which is quite larger than the experimentally observed frequency of β oscillations. However, we note that a small decrease of ~34 meV of Fermi energy reduces this frequency to 750 T, which is very close to the measured value, 705 T. In contrast, the calculated effective mass, $0.52m_e$ shows much better agreement with the measured value, $0.514m_e$. Meanwhile, the purple hole pockets have a more complex shape, which can give rise

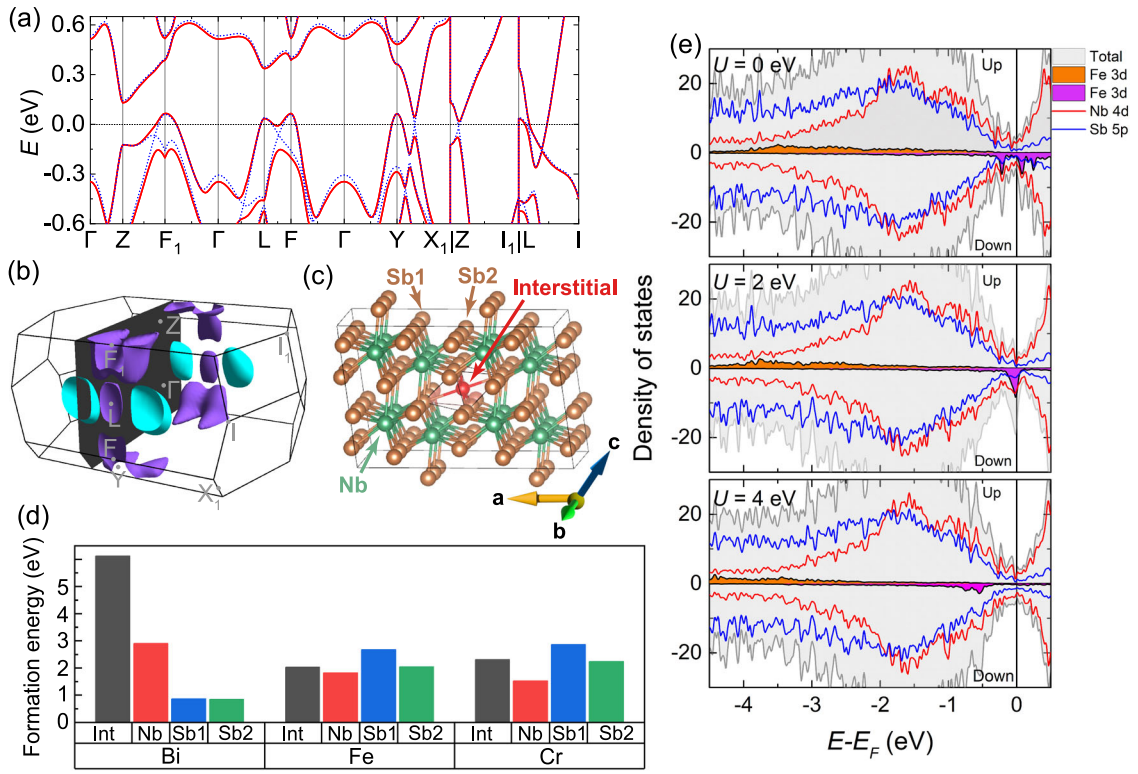

Fig. 5 Electronic structure of pristine and Fe-doped $NbSb_2$. **a** Electronic structure of $NbSb_2$ along the high-symmetry lines with spin-orbit coupling (the red solid lines) and without spin-orbit coupling (the blue dotted lines). **b** Fermi surfaces of $NbSb_2$. The cyan and purple colors indicate the electron and hole pockets, respectively. The dark grey plane represents a cross-section plane for the extremum cross-section area of an electron Fermi surface perpendicular to the crystal *b*-axis. **c** Supercell of Fe-$Nb_{24}Sb_{48}$ with a Fe atom in the interstitial site (Fe_{int}). **d** Formation energy of neutral defects. The defect sites correspond to the labels in **c**. **e** Projected density of states of Fe-$Nb_{24}Sb_{48}$ with Hubbard correction *U* for Fe 3*d* orbital. Spin up and down contributions are shown in the upper and lower panels for each *U*. Only dominant Fe 3*d*, Nb 4*d*, and Sb 5*p* are plotted.

to a complicated MQO pattern. For a magnetic field applied along the crystal *b*-axis, we identified three extremal cross-sections from these pockets that correspond to the measured ζ, α, and not observed η oscillations (Fig. S6). The corresponding frequencies and effective masses are 138, 476, 588 T and 0.68, 0.84, 1.46m_e, respectively. Note that the frequency of η oscillations is closer to that of α oscillations experimentally and overlaps with it[15], which is the reason for η oscillations being undetected with its large effective mass. The calculated effective mass of ζ oscillations is in excellent agreement with the experiment ($m_c = 0.66m_e$).

We then calculated formation energies[98] of various defects to understand why these exceptional phenomena arise only in the Fe-doped case. For Bi, Fe, and Cr dopants, we considered four types of defects: Nb-substitution, Sb1-substitution, Sb2-substitution, and interstitial site, as shown in Fig. 5c. The calculated formation energies of defects in Fig. 5d reveal that the preferred defect sites vary depending on the dopant species, which are ~0.85 eV for Bi_{Sb}, ~1.52 eV for Cr_{Nb}, and ~1.82 eV for Fe_{Nb}. For Fe, Fe_{Nb}, Fe_{Sb2}, and Fe_{int}, they have similar formation energies. This implies that these types of defects would coexist, in contrast to Cr, which strongly prefers Cr_{Nb}. Note that the formation energy of defects should be positive for the crystal to be stable[99].

We also found that Cr-doping can result in low total magnetization because the total magnetization is much lower than the magnetic moment of a Cr atom due to induced anti-parallel spins of nearby atoms (see Supplementary Note 4 for the details). Remarkably, the total magnetic moment per Cr of Cr-doped sample decreases as the doping ratio decreases, which might explain experimentally undetectable Cr magnetic moments in the extremely dilute limit. This contrasts with Fe-doping, which has slightly higher total magnetization than the magnetic moment of the Fe atom due to induced parallel spins (Table S4, and Figure S7). Note that the magnetic moment of Fe is calculated out to range from 1.8 to 3.4 μ_B, which is in good agreement with the experiment (3 μ_B). We then calculated PDOS for four probable sites of Fe and Cr-doping to investigate any potential causes for the phase shift (see Fig. S8). Among all four cases, the Fe_{int} model exhibits very different behaviors from the others and is predicted to show the largest spin-dependent scattering.

We only plot the PDOS of Fe_{int} cases, where the strongest spin-dependent scattering is expected. Near the Fermi level, the dominant contributions arise from Nb 4*d*, Sb 5*p*, and Fe 3*d* orbital. Also, there is a clear imbalance in the density of states for opposite spin states of Fe 3*d*, suggesting the localized magnetic moment of the Fe dopants which is estimated as ~2.3 μ_B. Interestingly, the PDOS for the minor spin of Fe 3*d* shows a large peak, especially near the Fermi level with a finite DOS at the Fermi level. Also, the PDOS of Nb 4*d* is notably affected by the Fe 3d, which implies hybridization between Nb 4*d* and Fe 3*d*, possibly mediated by Sb 5*p*. We further considered the correlation effect of localized 3*d* orbitals of Fe atom by applying the Hubbard U correction. As U increases from 0 to 4 eV, the Fe 3*d* peaks of up spin and down spin in the PDOS (Fig. 5e) became more separated, with the minority-spin peak shifting further below the Fermi level. Besides, the local magnetic moment of Fe systematically grows from ~2.31μ_B at $U = 0$ eV to ~2.39 μ_B at $U = 2$ eV and to ~2.49 μ_B at $U = 4$ eV. In addition, at $U = 2$ eV, the DOS of Fe 3 *d* minority spin has a large peak at the Fermi level with ~100 meV width, for which further hybridization between the localized orbital and the conduction electron bath builds when the scope of the Anderson impurity model is adopted. These results may support the notable deviation of the scattering rate between each spin.

Ethics approval and consent to participate

All methods were carried out in accordance with the relevant guidelines and regulations. This study did not involve human participants, human data, or live vertebrate animals. Therefore, ethical approval and informed consent to participate were not required.

Conclusions

In this study, we observed a significant phase deviation of the dHvA effect induced by dilute magnetic doping of Fe, approximately 34 ppm per formula unit. The high sensitivity of the ultraclean host material to the introduction of magnetic impurities allows us to detect this subtle effect. The considerable phase deviation is well fitted with the spin-dependent scattering model. The DFT calculation for Fe-doped $NbSb_2$ reveals an imbalance of occupation between the opposite spins, confirming the localized magnetic moments of Fe dopants. Importantly, we found the peak in the density of states for the minor spin states near the Fermi level, which is aligned with the spin-dependent scattering rate and the active interaction between the localized magnetic moment and the itinerant electron observed in Fe-doped $NbSb_2$. Our study demonstrates that even an extremely small amount of magnetic impurities could give a considerable phase deviation in the dHvA effects, giving insight into the phase interpretation of MQOs, as well as the fundamental understanding of the interaction between itinerant electrons and magnetic impurities.

Acknowledgements

This work was supported by the National Research Foundation of Korea (NRF) (Grant Nos. RS202500516322, RS202500512822, and RS2022NR068225) and the National Research Council of Science & Technology (NST) grant by the Korea government (MIST) (Grant No. GTL 25091–102). A portion of this work was performed at the National High Magnetic Field Laboratory, which is supported by National Science Foundation Cooperative Agreement No. DMR-2128556* and the State of Florida. RECMIB is supported by the State of Florida.

Author details

[1]Department of Physics, Sogang University, Seoul, Republic of Korea. [2]National High Magnetic Field Laboratory, Tallahassee, FL, USA. [3]Department of Materials Science and Engineering, Yonsei University, Seoul, Republic of Korea. [4]Center for Rare Earths, Critical Minerals, and Industrial Byproducts (RECMIB), National High Magnetic Field Laboratory, Tallahassee, FL, USA. [5]Department of Earth, Ocean and Atmospheric Science, Florida State University, Tallahassee, FL, USA

Author contributions

S.-E.L. and S.J. contributed equally to this work. S.-E.L. and M.-H.J. devised the concept. S.-E.L. synthesized the crystals, measured electrical and magnetic properties, and analyzed the data. S.J. conducted the DFT calculations. J.P. and M.H. conducted μXRF measurements. The interpretation of data, analyses, and calculations was actively discussed between all authors. M.-H.J. supervised this research. The manuscript was written by S.-E.L and S.J. M.-H.J. edited the manuscript.

Competing interests

The authors declare no competing interests.

Publisher's note

Springer Nature remains neutral with regard to jurisdictional claims in published maps and institutional affiliations.

Supplementary information The online version contains supplementary material available at https://doi.org/10.1038/s41427-026-00650-x.

Received: 9 July 2025 Revised: 17 March 2026 Accepted: 27 March 2026
Published online: 22 April 2026

References

1. Yelland, E. A. et al. Quantum oscillations in the underdoped cuprate $YBa_2Cu_4O_8$. *Phys. Rev. Lett.* **100**, 047003 (2008).
2. Coldea, A. I. et al. Fermi surface of superconducting LaFePO determined from quantum oscillations. *Phys. Rev. Lett.* **101**, 216402 (2008).
3. Van Der Wel, P. J. et al. Quantum oscillations near B_{c2} in the Organic Superconductor κ-$(BEDT\text{-}TTF)_2Cu(NCS)_2$. *Phys. C* **235**, 2453–2454 (1994).
4. Doiron-Leyraud, N. et al. Quantum oscillations and the Fermi surface in an underdoped high-T_c superconductor. *Nature* **447**, 565–568 (2007).
5. Weiss, H. et al. Magnetic quantum oscillations in the organic superconductor κ-$(BEDT\text{-}TTF)_2Cu[N(CN)_2]$. *Br. J. Exp. Theor. Phys.* **66**, 202–207 (1997).
6. Barišić, N. et al. Universal quantum oscillations in the underdoped cuprate superconductors. *Nat. Phys.* **9**, 761–764 (2013).
7. Wang, J. et al. Vanishing quantum oscillations in Dirac semimetal ZrTe. *Proc. Natl. Acad. Sci. USA* **115**, 9145–9150 (2018).
8. Orbanić, F., Novak, M., Baćani, M. & Kokanović, I. Quantum oscillations in a lead chalcogenide three-dimensional Dirac system. *Phys. Rev. B* **95**, 035208 (2017).
9. Jiang, Q. et al. Quantum oscillations in the field-induced ferromagnetic state of $MnBi_{2-x}Sb_xTe_4$. *Phys. Rev. B* **103**, 205111 (2021).
10. Zhao, W. et al. Quantum oscillations in iron-doped single crystals of the topological insulator Sb_2Te_3. *Phys. Rev. B* **99**, 165133 (2019).
11. Qu, D. X., Hor, Y. S., Xiong, J., Cava, R. J. & Ong, N. P. Quantum oscillations and Hall anomaly of surface states in the topological insulator Bi_2Te_3. *Science* **329**, 821–824 (2010).

12. Ren, Z., Taskin, A. A., Sasaki, S., Segawa, K. & Ando, Y. Large bulk resistivity and surface quantum oscillations in the topological insulator Bi_2Te_2Se. *Phys. Rev. B* **82**, 241306(R) (2010).
13. Zhao, K. et al. Magnetic tuning of band topology evidenced by exotic quantum oscillations in the Dirac semimetal $EuMnSb_2$. *Phys. Rev. B* **107**, L081112 (2023).
14. Xiong, J. et al. Quantum oscillations in a topological insulator Bi_2Te_2Se with large bulk resistivity (6 Ω cm). *Phys. E* **44**, 917–920 (2012).
15. Lee, S.-E. et al. Orbit topology analyzed from π phase shift of magnetic quantum oscillations in three-dimensional Dirac semimetal. *Proc. Natl. Acad. Sci. USA* **118**, e2023027118 (2021).
16. Moll, P. J. W. et al. Transport evidence for Fermi-arc-mediated chirality transfer in the Dirac semimetal Cd_3As_2. *Nature* **535**, 266–270 (2016).
17. Pereg-Barnea, T., Weber, H., Refael, G. & Franz, M. Quantum oscillations from Fermi arcs. *Nat. Phys.* **6**, 44–49 (2010).
18. Xiang, Z. et al. Quantum oscillations of electrical resistivity in an insulator. *Science* **362**, 65–69 (2018).
19. Knolle, J. & Cooper, N. R. Quantum oscillations without a fermi surface and the anomalous de Haas-van Alphen effect. *Phys. Rev. Lett.* **115,** 146401 (2015).
20. Bi, R. et al. Spin zero and large Landé g-factor in WTe_2. *New J. Phys.* **20**, 063026 (2018).
21. Mikitik, G. P. & Sharlai, Y. V. G. factor of conduction electrons in the de Haas-van Alphen effect. *Phys. Rev. B* **65**, 1–10 (2002).
22. Cohen, M. H. & Blount, E. I. The g-factor and de Haas-van Alphen effect of electrons in bismuth. *Philos. Mag.* **5**, 115–126 (1960).
23. Mikitik, G. P. & Sharlai, Y. V. The Berry phase in graphene and graphite multilayers. *Fiz. Nizk. Temp.* **34**, 1012–1019 (2008).
24. Zhang, Y., Tan, Y. W., Stormer, H. L. & Kim, P. Experimental observation of the quantum Hall effect and Berry's phase in graphene. *Nature* **438**, 201–204 (2005).
25. Fang, L. et al. Catalyst-free growth of millimeter-long topological insulator Bi_2Se_3 nanoribbons and the observation of the π-berry phase. *Nano Lett.* **12**, 6164–6169 (2012).
26. Taskin, A. A., Sasaki, S., Segawa, K. & Ando, Y. Manifestation of topological protection in transport properties of epitaxial Bi_2Se_3 thin films. *Phys. Rev. Lett.* **109**, 066803 (2012).
27. Kim, S. W. et al. Effect of antiferromagnetic order on topological electronic structure in Eu-substituted Bi_2Se_3 single crystals. *APL Mater.* **8**, 111108 (2020).
28. Jun, J. H., Kim, J., Kim, S. W. & Jung, M. H. Signature of topological states in antiferromagnetic Sm-substituted Bi_2Te_3. *Sci. Rep.* **10**, 9615 (2020).
29. Kim, S. W. & Jung, M. H. Electronic properties of $Gd_xBi_{2-x}Se_3$ single crystals analyzed by Shubnikov-de Haas oscillations. *Appl. Phys. Lett.* **112**, 202401 (2018).
30. Ji, S., Lee, S. E. & Jung, M. H. Berry paramagnetism in the Dirac semimetal $ZrTe_5$. *Commun. Phys.* **4**, 265 (2021).
31. Liang, T. et al. Ultrahigh mobility and giant magnetoresistance in the Dirac semimetal Cd_3As_2. *Nat. Mater.* **14**, 280–284 (2015).
32. He, L. P. et al. Quantum transport evidence for the three-dimensional dirac semimetal phase in Cd_3As_2. *Phys. Rev. Lett.* **113**, 246402 (2014).
33. Xiang, Z. J. et al. Angular-dependent phase factor of Shubnikov-de Haas oscillations in the Dirac semimetal Cd_3As_2. *Phys. Rev. Lett.* **115**, 226401 (2015).
34. Liu, Y. et al. Zeeman splitting and dynamical mass generation in Dirac semimetal ZrTe. *Nat. Commun.* **7**, 12516 (2016).
35. Sergelius, P. et al. Berry phase and band structure analysis of the Weyl semimetal NbP. *Sci. Rep.* **6**, 33859 (2016).
36. Hu, J. et al. φ Berry phase and Zeeman splitting of Weyl semimetal. *TaP. Sci. Rep.* **6**, 18674 (2016).
37. Alexandradinata, A., Wang, C., Duan, W. & Glazman, L. Revealing the topology of fermi-surface wave functions from magnetic quantum oscillations. *Phys. Rev. X* **8**, 011027 (2018).
38. Gao, Y. & Niu, Q. Zero-field magnetic response functions in Landau levels. *Proc. Natl. Acad. Sci. USA* **114**, 7295–7300 (2017).
39. Datta, B. et al. Nontrivial quantum oscillation geometric phase shift in a trivial band. *Sci. Adv.* **5**, eaax6550 (2019).
40. Lee, S.-E. & Jung, M.-H. Inhomogeneity identification by measuring magnetic quantum oscillations. *Phys. B* **670**, 415321 (2023).
41. Lubczynskit, W., Cisowskit, J., Kossutz, J. & Portals, J. C. Spin-dependent scattering of conduction electrons in $Cd_{3-x-y}Zn_xMn_yAs_2$ alloys. *Semicond. Sci. Technol.* **6**, 619–625 (1991).
42. Vaziri, M. & Reifenberger, R. Spin-dependent scattering of conduction electrons in diluted magnetic semiconductors: $Hg_{1-x}Fe_xSe$. *Phys. Rev. B* **32**, 3921–3929 (1985).
43. Akimov, B. A., Lvova, N. A. & Ryabova, L. I. Quantum oscillatory properties of the semimagnetic semiconductor PbTe(Cr). *Phys. Rev. B* **58**, 10430 (1998).
44. Wang, K., Graf, D., Li, L., Wang, L. & Petrovic, C. Anisotropic giant magnetoresistance in NbSb. *Sci. Rep.* **4**, 7328 (2014).
45. Li, P. et al. Colossal Nernst power factor in topological semimetal NbSb. *Nat. Commun.* **13**, 1762 (2022).
46. Reddy, M. A. & Varadaraju, U. V. $NbSb_2$ as an anode material for Li-ion batteries. *J. Power Sources* **159**, 336–339 (2006).
47. Guo, L. et al. Extreme magnetoresistance and SdH oscillation in compensated semimetals of $NbSb_2$ single crystals. *J. Appl. Phys.* **123**, 155103 (2018).
48. Carnimeo, I. et al. Quantum ESPRESSO: one further step toward the exascale. *J. Chem. Theory Comput.* **19**, 6992–7006 (2023).
49. Giannozzi, P. et al. Advanced capabilities for materials modelling with quantum ESPRESSO. *J. Phys. Condens. Matter* **29,** 465901 (2017).
50. Giannozzi, P. et al. QUANTUM ESPRESSO: a modular and open-source software project for quantum simulations of materials. *J. Phys. Condens. Matter* **21**, 395502 (2009).
51. Perdew, J. P. & Zunger, A. Self-interaction correction to density-functional approximations for many-electron systems. *Phys. Rev. B* **23**, 5048 (1981).
52. Perdew, J. P. et al. Atoms, molecules, solids, and surfaces: applications of the generalized gradient approximation for exchange and correlation. *Phys. Rev. B* **48**, 4978 (1993).
53. Kresse, G. & Joubert, D. From ultrasoft pseudopotentials to the projector augmented-wave method. *Phys. Rev. B* **59**, 1758 (1999).
54. Dal Corso, A. Pseudopotentials periodic table: From H to Pu. *Comput. Mater. Sci.* **95**, 337–350 (2014).
55. Monkhorst, H. J. & Pack, J. D. Special points for Brillouin-zone integrations. *Phys. Rev. B* **13**, 5188 (1976).
56. Karn, N. K. et al. Magneto-transport and first principle study of strong topological insulator gray-arsenic. *Mater. Res. Express* **12**, 036301 (2025).
57. Rourke, P. M. C. & Julian, S. R. Numerical extraction of de Haas–van Alphen frequencies from calculated band energies. *Comput. Phys. Commun.* **183**, 324–332 (2012).
58. van Setten, M. J. et al. The PseudoDojo: training and grading a 85 element optimized norm-conserving pseudopotential table. *Comput. Phys. Commun.* **226**, 39–54 (2018).
59. Liechtenstein, A. I., Anisimov, V. I. & Zaanen, J. Density-functional theory and strong interactions: orbital ordering in Mott-Hubbard insulators. *Phys. Rev. B* **52**, R5467(R) (1995).
60. Momma, K. & Izumi, F. VESTA 3 for three-dimensional visualization of crystal, volumetric and morphology data. *J. Appl. Crystallogr.* **44**, 1272–1276 (2011).
61. Kawamura, M. FermiSurfer: fermi-surface viewer providing multiple representation schemes. *Comput. Phys. Commun.* **239**, 197–203 (2019).
62. Leahy, I. A. et al. Nonsaturating large magnetoresistance in semimetals. *Proc. Natl. Acad. Sci. USA* **115**, 10570–10575 (2018).
63. Ashcroft, N. W. & Mermin, N. D. *Solid State Physics* (Saunders College Publishing, 1976).
64. Chen, W., Lu, H. Z. & Zilberberg, O. Weak localization and antilocalization in nodal-line semimetals: dimensionality and topological effects. *Phys. Rev. Lett.* **122**, 196603 (2019).
65. Fu, B., Wang, H. W. & Shen, S. Q. Quantum interference theory of magnetoresistance in Dirac materials. *Phys. Rev. Lett.* **122**, 246601 (2019).
66. Nakamura, H. et al. Robust weak antilocalization due to spin-orbital entanglement in Dirac material Sr_3SnO. *Nat. Commun.* **11**, 1161 (2020).
67. Salawu, Y. A., Yun, J. H., Rhyee, J.-S., Sasaki, M. & Kim, H.-J. Weak antilocalization, spin–orbit interaction, and phase coherence length of a Dirac semimetal $Bi_{0.97}Sb_{0.03}$. *Sci. Rep.* **12**, 2845 (2022).
68. Song, J. C. W., Refael, G. & Lee, P. A. Linear magnetoresistance in metals: Guiding center diffusion in a smooth random potential. *Phys. Rev. B* **92**, 180204 (2015).
69. Nagaosa, N., Sinova, J., Onoda, S., MacDonald, A. H. & Ong, N. P. Anomalous Hall effect. *Rev. Mod. Phys.* **82**, 1539–1592 (2010).
70. Xu, C. et al. Electronic structures of transition metal dipnictides XPn_2 (X=Ta, Nb; Pn= P, As, Sb). *Phys. Rev. B* **93**, 195106 (2016).
71. Ali, M. N. et al. Large, non-saturating magnetoresistance in WTe_2. *Nature* **514**, 205–208 (2014).
72. Kumar, N. et al. Extremely high magnetoresistance and conductivity in the type-II Weyl semimetals WP_2 and MoP_2. *Nat. Commun.* **8**, 1642 (2017).

73. Singha, R., Pariari, A. K., Satpati, B. & Mandal, P. Large nonsaturating magnetoresistance and signature of nondegenerate Dirac nodes in ZrSiS. *Proc. Natl. Acad. Sci. USA* **114**, 2468–2473 (2017).
74. Guo, L. et al. Electronic transport properties of $Nb_{1-x}Ta_xSb_2$ single-crystal semimetals grown by a chemical vapor transport based high-throughput method. *Cryst. Growth Des.* **21**, 653–662 (2021).
75. Kondo, J. Resistance minimum in dilute magnetic alloys. *Prog. Theor. Phys.* **32**, 37–49 (1964).
76. Hewson, A. C. *The Kondo Problem to Heavy Fermions* (Cambridge University Press, 1993). https://doi.org/10.1017/CBO9780511470752.
77. Kouwenhoven, L. & Glazman, L. Revival of the Kondo effect. *Phys. World* **14**, 33–38 (2001).
78. Jang, S. et al. Evolution of the Kondo lattice electronic structure above the transport coherence temperature. *Proc. Natl. Acad. Sci. USA* **117**, 23467–23476 (2020).
79. Nakatsuji, S. et al. Intersite coupling effects in a Kondo lattice. *Phys. Rev. Lett.* **89**, 106402 (2002).
80. Pikul, A. P. et al. Single-ion Kondo scaling of the coherent Fermi liquid regime in $Ce_{1-x}La_xNi_2Ge_2$. *Phys. Rev. Lett.* **108**, 066405 (2012).
81. Im, H. et al. Observation of Kondo condensation in a degenerately doped silicon metal. *Nat. Phys.* **19**, 676–681 (2023).
82. Anderson, P. W. Localized magnetic states in metals. *Phys. Rev.* **124**, 41–53 (1961).
83. Schrieffer, J. R. & WoLzz, P. A. Relation between the Anderson and Kondo Hamiltonians. *Phys. Rev.* **149**, 491–492 (1966).
84. Ruderman, M. A. & Kittel, C. Indirect exchange coupling of nuclear magnetic moments by conduction electrons. *Phys. Rev.* **96**, 99–102 (1954).
85. Kasuya, T. A Theory of metallic ferro- and antiferromagnetism on Zener's model. *Prog. Theor. Phys.* **16**, 45–57 (1956).
86. Yosida, K. Magnetic properties of Cu-Mn alloys. *Phys. Rev.* **106**, 893–898 (1957).
87. Dellby, B. Kondo Temperature and magnetic moment from susceptibility data on dilute alloys. *Phys. Status Solidi* **35**, K147–K149 (1969).
88. Barua, S., Hatnean, M. C., Lees, M. R. & Balakrishnan, G. Signatures of the Kondo effect in VSe. *Sci. Rep.* **7**, 10964 (2017).
89. Deng, X. et al. Signatures of Mottness and Hundness in archetypal correlated metals. *Nat. Commun.* **10**, 1433 (2019).
90. Ding, X. et al. Crossover from Kondo to Fermi-liquid behavior induced by high magnetic field in 1T- VTe_2 single crystals. *Phys. Rev. B* **103**, 125115 (2021).
91. Huang, B., Yang, Y. F. & Wang, W. H. Kondo effect and non-Fermi liquid behavior in metallic glasses containing Yb, Ce, and Sm. *J. Appl. Phys.* **113**, 163505 (2013).
92. Liu, H. et al. Observation of the Kondo effect in multilayer single-crystalline VTe_2 nanoplates. *Nano Lett.* **19**, 8572–8580 (2019).
93. Onsager, L. Interpretation of the de Haas-van Alphen effect. *Phil. Mag.* **43**, 1006–1008 (1952).
94. Shoenberg, D. *Magnetic Oscillations in Metals* (Cambridge University Press, Cambridge, 1984).
95. Quantum Design. *Application Note 1070-207: Using PPMS Superconducting Magnets at Low Fields* (Quantum Design, 2009).
96. Ren, Z., Taskin, A. A., Sasaki, S., Segawa, K. & Ando, Y. Fermi level tuning and a large activation gap achieved in the topological insulator Bi_2Te_2Se by Sn doping. *Phys. Rev. B* **85**, 155301 (2012).
97. Brailspord, A. D. Influence of Impurities on the de Haas-van Alphen effect. *Phys. Rev.* **149**, 456–463 (1966).
98. Freysoldt, C. et al. First-principles calculations for point defects in solids. *Rev. Mod. Phys.* **86**, 253–305 (2014).